Simulation of Cyclic Loading on Pipe Elbows Using Advanced Plane-Stress Elastoplasticity Models

Simulation of Cyclic Loading on Pipe Elbows using Advanced Plane-Stress Elasto-plasticity Models[1]

Konstantinos Chatziioannou
School of Engineering,
The University of Edinburgh,
Edinburgh, Scotland, UK

Yuner Huang
School of Engineering,
The University of Edinburgh,
Edinburgh, Scotland, UK

Spyros A. Karamanos[2]
Department of Mechanical Engineering,
University of Thessaly,
Volos, Greece
Email: skara@mie.uth.gr

Abstract

The present work investigates the response of industrial steel pipe elbows subjected to severe cyclic loading (e.g. seismic or shutdown/startup conditions), associated with the development of significant inelastic strain amplitudes of alternate sign, which may lead to low-cycle fatigue. To model this response, three cyclic-plasticity hardening models are employed for the numerical analysis of large-scale experiments on elbows reported elsewhere. The constitutive relations of the material model follow the context of von Mises cyclic elasto-plasticity, and the hardening models are implemented in a user subroutine, developed by the authors, which employs a robust numerical integration scheme, and is inserted in a general-purpose finite element software. The three hardening models are evaluated in terms of their ability to predict the strain range at critical locations, and in particular, strain accumulation over the load cycles, a phenomenon called "ratcheting". The overall good comparison between numerical and experimental results demonstrates that the proposed numerical methodology can be used for simulating accurately the mechanical response of pipe elbows under severe inelastic repeated loading. Finally, the paper highlights some limitations of conventional hardening rules in simulating multi-axial material ratcheting.

[1] *Presented in an early form in the ASME2019 PVP Conference, San Antonio, Texas, Paper No. PVP2019-93507*

[2] *Formerly: School of Engineering, The University of Edinburgh, Edinburgh, Scotland, UK*

1. Introduction

Metal pipe elbows are widely used in industrial applications such as power plants (nuclear or fossil), chemical and petrochemical facilities, or gas and oil terminals. As a result, their structural integrity is crucial for the safe operation of the industrial facility. Under severe external actions, such as earthquakes or shutdowns/startups, steel pipe elbows are imposed to strong cyclic loading conditions and may fail due to low-cycle fatigue [1][2]. Under such strong loading conditions, the inelastic response may be accompanied by progressive accumulation of plastic deformations or strains, a phenomenon known as "ratcheting". This phenomenon results into early low-cycle fatigue cracking [3–5] or structural collapse [6,7].

Previous experimental studies have contributed to better understanding the evolution of strain in pipe elbows. Moreton *et al*. [8] determined experimentally the minimum in-plane cyclic bending moment necessary to initiate ratcheting, whereas Yahiaoui *et al.* [9][10] identified the principal direction of ratcheting (hoop or axial) in pipe elbows under in- and out-of-plane cyclic bending. Further experimental results on pipe elbows subjected to seismic loading conditions have been reported by Slagis [11]. Using a shaking table, 32 piping components have been tested to quantify the impact of fabrication details on the structural performance under seismic loading. Suzuki *et al*. [12] reported the experimental results of a 6-year project aiming at evaluating fatigue damage under severe seismic loading, and more recently Chen *et al*. [13] tested steel pipe elbows under constant internal pressure and cyclic in-plane bending. Pipe wall thinning effects have been investigated by Shi *et. al* [14] and demonstrated that ratcheting occurs mainly in the hoop direction, while the ratcheting rate grows proportionally with the increase of the applied cyclic-bending amplitude or the internal pressure. Vishnuvardhan *et al*. [15] and Varelis *et al*. [16][17] reported additional experimental results concerning the cyclic response of pipe elbows. In these studies, low-cycle fatigue failure was due to the development of through-thickness cracking, followed by a pipe cross-section ovalization at the bend. In addition, Varelis *et al*. [16][17] compared the experimental results with design code provisions, highlighting the conservativeness of current design tools in predicting the number of cycles to failure.

Despite the existence of test data, as described above, and the recent advancements in cyclic plasticity, the numerical simulation of material ratcheting is still a challenging topic [18–20]. An extensive literature review discussing relevant approaches and limitations can be found in the paper by Chen *et al*. [21]. In particular, the choice of hardening rule has been pinpointed as the key issue for predicting ratcheting. Bari and Hassan [22][23] assessed the accuracy of five hardening models in simulating ratcheting on piping components, whereas in subsequent publication [24], they proposed modifications on the evolution law of the nonlinear hardening rule [25], in an attempt to simulate multi-axial ratcheting evolution in steel pipes.

Ayob *et al*. [26] and Balan and Redektop [27] analysed pressurized steel pipe elbows under in-plane cyclic bending with or without thinning effects, whereas shakedown limit loads were numerically computed by Oh *et al*. [28]. More recently, Varelis *et al*. [16][17] presented results from numerical simulations on steel pipe elbows under inelastic loading, implementing in the finite element environment the bounding-surface cyclic-plasticity model initially proposed by Tseng and Lee [29]. Furthermore, Hassan and Rahman [30] and Rahman *et al*. [31] simulated experiments on piping under cyclic inelastic loading, using several advanced hardening models, towards ratcheting predictions. The results indicated the strengths and weaknesses of each constitutive model, and demonstrated the capability of the kinematic hardening rule proposed by Bari and Hassan [24] in simulating multi-axial ratcheting evolution. In a more recent paper, Hassan and Rahman [32] employed seven kinematic hardening models to simulate ratcheting experiments on pipe elbows reported in [33]. They calibrated the hardening rules using uni-axial and multi-axial material tests, showing that advanced kinematic hardening rules such as those proposed in [24] and [34] may predict more accurately the strain increase rate observed experimentally, especially at the elbow flank. Nevertheless, the predicted ratcheting rate at the elbow intrados and the extrados did not compare well with the test results, and this was attributed to the inability of the constitutive models to properly describe the yield surface evolution due to cyclic loading. Very recently, Islam and Hassan [35] enhanced the kinematic hardening rule proposed in [24] to improve ratcheting predictions on pipe elbows by introducing (a) a strain-range-dependent shape hardening parameter which also accounts for non-proportional loading and (b), a multi-axial ratcheting parameter that evolves according to the size of a strain-memory surface. Using this enhanced hardening rule, Islam and Hassan [35] predicted quite accurately the experimental data in [33][36]. The main conclusion from the previous studies is that the use of appropriate numerical tools, which employ advanced hardening rules, are required for assessing the structural performance of piping under severe cyclic loading leading to low-cycle fatigue. Towards that purpose, the reliable prediction of strain ratcheting is shown to be of paramount importance [37,38].

Previous studies [22–24] have shown that "built-in" material models in commercial finite element software may not be able to simulate accurately stain ratcheting, and therefore, in-house implementation of special-purpose material models is required. Towards this purpose, an implicit numerical integration scheme has been developed recently by the authors on the basis of J_2 cyclic elasto-plasticity with combined nonlinear hardening, capable of integrating a wide range of cyclic plasticity models and hardening rules under a common computational framework [39]. The numerical scheme accounts explicitly for plane stress conditions, suitable for simulating the mechanical response of piping and other thin-walled structural components using shell

type elements. This implicit integration scheme has been presented extensively in [39], together with the corresponding consistent linearization moduli, and its implementation in the finite element software ABAQUS [40].

The current work employs the numerical model presented and validated by the authors in [39], and examines the capabilities of three advanced cyclic plasticity hardening rules in simulating multi-axial ratcheting measured in physical experiments. A set of large-scale experiments on steel pipe elbows subjected to strong cyclic loading, presented elsewhere [41], are considered and simulated numerically to predict their mechanical behavior in terms of force-displacement response, local strain range and accumulation and the corresponding cross-sectional ovalization. The numerical results highlight the capabilities of the three hardening rules under consideration and pinpoint some key issues associated with the simulation of ratcheting in pipe elbows.

The present paper is structured in the following manner. After an outline of the experimental program under consideration [41] in Section 2, the main features of the numerical scheme employed are highlighted in Section 3, and issues related to the numerical implementation of the material model in a finite element environment and the calibration of the three hardening models are addressed. Subsequently in Section 4, the finite element model is presented, followed by numerical results and their comparison with the experimental data. Finally, in the last section of the paper, the most important conclusions are summarized and discussed.

2. Outline of the experimental program

Physical experiments on steel pipe elbows have been performed under severe in-plane cyclic bending at Delft University of Technology in the course of a large European research program [41]. The specimens and the corresponding testing parameters of each pipe elbow specimen are summarized in Table 1 where, for consistency reasons, the specimens are labelled as in [41]. The specimens consist of 8-inch-diameter SCH40 long-radius induction bends [42], butt-welded to two straight parts. Each straight part has a length equal to five times the diameter (1100mm) of the pipe. The nominal diameter D and thickness t are equal to 219.1mm and 8.18mm respectively, and the nominal bend ratio is R/D=1.5, where R is the bend radius. The thickness of the specimens was measured prior to testing, indicating variations on the pipe bend thickness, which could be up to 25% higher than the nominal value, especially at the intrados area. The base material is P355N according to European (EN) 10216 standards, which is the EN equivalent of API 5L X52. Monotonic tensile material tests on coupon specimens extracted from similar bends of the same heat shown 0.2% yield strength and ultimate strength of 396MPa and 543MPa, respectively [41]. A schematic representation of the experimental set-up is presented in Figure 1(a). The ends of the straight pipe segments are capped with steel plates, welded on the specimen. The specimen is loaded through a horizontal hydraulic actuator connected to

one end of the specimen with a hinge, while the other end is pin-supported. The specimens are subjected to displacement-control in-plane cyclic bending up to failure, in the form of through-wall cracking at the elbow flank. A very small level of internal pressure, equal to 1 bar, is applied in the specimens during testing to detect the development of through-thickness crack. This low pressure is neglected in the numerical calculations. Hoop strain measurements are recorded during testing using strain gauges of dimensions 10mm × 1mm. Figure 1(b) shows the location of the five strain gauges used at the elbow flank to measure hoop strains. Strain gauge 5 is located exactly at the flank, while the distance between adjacent strain gauges is equal to 3mm and 6mm in the axial and the hoop direction, respectively.

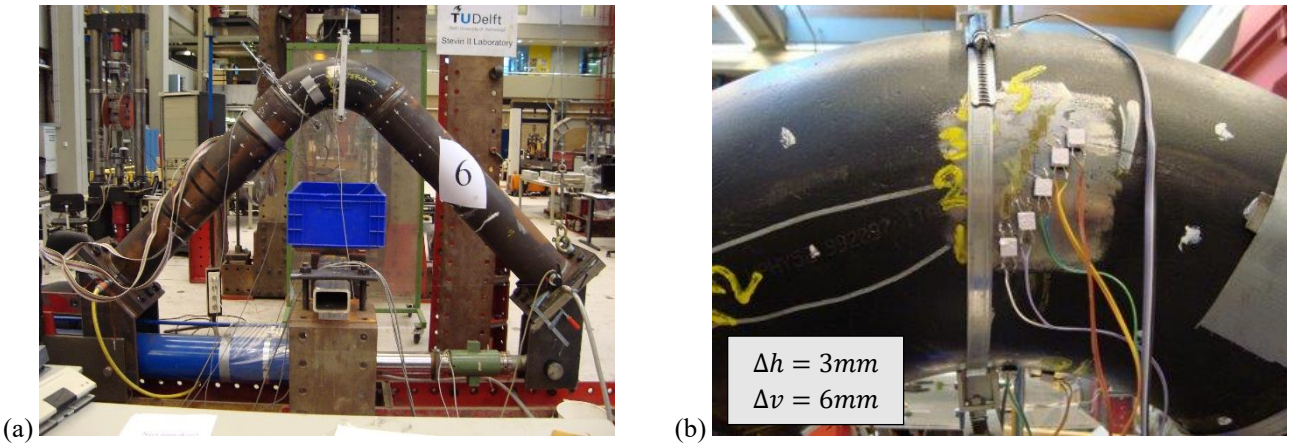

Figure 1: (a) Experimental set-up of the elbow specimen, (b) Location of strain gauges [41].

Table 1: Testing conditions

Test	*E2*	*E3*	*E4*	*E5*	*E6*	*E7*	*E8*
Displacement amplitude (mm)	±70	±100	±150	±200	±250	±300	Increasing amplitude
Number of cycles to failure	444	171	61	28	16	10	16

3. Constitutive model

The constitutive equations of the cyclic-plasticity model, and their implementation within the finite element environment have been extensively presented in [39], but some key information are summarized in this section for the sake of completeness.

3.1 Model formulation

The constitutive relations of the present numerical scheme are formulated on the basis of J_2 plane stress cyclic elasto-plasticity with mixed nonlinear hardening. The model was developed by extending the methodology proposed by Simo and Taylor [43] for classical plane stress elasto-plasticity. Using the projection matrix tensor $\boldsymbol{P}$ [43], the governing equations obtain the following form:

$$\boldsymbol{\varepsilon} = \boldsymbol{\varepsilon}^e + \boldsymbol{\varepsilon}^p \tag{1}$$

$$\boldsymbol{\sigma} = \boldsymbol{M}\boldsymbol{\varepsilon}^e \tag{2}$$

$$\boldsymbol{\xi} = \boldsymbol{\sigma} - \boldsymbol{\alpha} \tag{3}$$

$$f = \sqrt{\boldsymbol{\xi}\boldsymbol{P}\boldsymbol{\xi}} - \sqrt{2/3}\, k(\varepsilon^q) \leq 0 \tag{4}$$

where $\boldsymbol{\varepsilon}$ $[\varepsilon_{11}\ \varepsilon_{22}\ 2\varepsilon_{12}]^t$ is the total strain tensor and its in-plane components, $\boldsymbol{\varepsilon}^e$ $[\varepsilon^e{}_{11}\ \varepsilon^e{}_{22}\ 2\varepsilon^e{}_{12}]^t$ is the elastic strain tensor and $\boldsymbol{\varepsilon}^p$ $[\varepsilon^p{}_{11}\ \varepsilon^p{}_{22}\ 2\varepsilon^p{}_{12}]^t$ is the plastic strain tensor, expressed in Voigt notation. Components $\varepsilon_{33}, \varepsilon^e{}_{33}$ and $\varepsilon^p{}_{33}$ are not included in the above tensors as these are dependent variables, computed from the plane stress requirement and the condition of isochoric plastic flow. For an isotropic material such as steel, this leads to

$$\varepsilon^e{}_{33} = -\nu(\varepsilon^e{}_{11} + \varepsilon^e{}_{22}),\ \varepsilon^p{}_{33} = -\varepsilon^p{}_{11} - \varepsilon^p{}_{22} \tag{5}$$

In Eq. (2), $\boldsymbol{M}$ is the (3×3) elastic constitutive matrix expressed in the plane stress domain, and ν is Poisson's ratio. Furthermore, $\boldsymbol{\sigma}$ $[\sigma_{11}\,\sigma_{22}\,\sigma_{12}]^t$, $\boldsymbol{\alpha}$ $[a_{11}\ a_{22}\ a_{12}]^t$ are the stress tensor and the back-stress tensor. Plane stress requires $\sigma_{33} = a_{33} = 0$ and thus, these terms are not considered in the vector notations of the stress and the back-stress tensors. The von Mises yield function (f) is expressed in Eq. (4), whereas the evolution of the yield surface size is described by the isotropic hardening rule $k(\varepsilon^q)$, which is a function of the equivalent plastic strain ε^q, defined as $\varepsilon^q = \sqrt{2/3\boldsymbol{\varepsilon}^p \cdot \boldsymbol{\varepsilon}^p}$. The plastic strain tensor $\boldsymbol{\varepsilon}^p$ is obtained in rate form using associative plasticity as:

$$\dot{\boldsymbol{\varepsilon}}^p = \dot{\lambda}\frac{\partial F}{\partial \boldsymbol{\sigma}} = \dot{\lambda}\boldsymbol{P}\boldsymbol{\xi} \tag{6}$$

where $\dot{\lambda}$ is the plastic multiplier. The following isotropic hardening function is adopted:

$$k(\varepsilon^q) = \sigma_y + Q(1 - e^{-b\varepsilon^q}) \tag{7}$$

where, σ_y is the initial size of the yield surface, and Q, b are material parameters.

The kinematic hardening rule is the key point of this formulation. Previous numerical results [24,35] have shown that accurate simulation of ratcheting requires enhancements of the classical nonlinear kinematic hardening rule, proposed initially by Armstrong and Frederick [25], and in a more generalized form by Chaboche [44]. Therefore, in the present numerical scheme, kinematic hardening is expressed in a general form with multiple (N) modified back-stresses as:

$$\dot{\boldsymbol{a}} = \sum_{i=1}^{N} (\dot{\boldsymbol{a}}^i) \tag{8}$$

where,

$$\dot{\boldsymbol{a}}^i = C_i\dot{\boldsymbol{\varepsilon}}^p - \gamma_i[\boldsymbol{a}^i\delta_i + (1-\delta_i)(\boldsymbol{a}^i \cdot \boldsymbol{n})\boldsymbol{n}]\dot{\varepsilon}^q \left\langle 1 - \frac{\overline{a_i}}{f(\boldsymbol{a}^i)} \right\rangle \tag{9}$$

$C_i, \gamma_i, \delta_i, \chi_i, \overline{a_i}$ are material parameters of the i back-stress tensor to be determined from appropriate cyclic material tests [24][31]. In Eq. (9), $f(\boldsymbol{a}^i) = \sqrt{\boldsymbol{a}^i \cdot \boldsymbol{P} \cdot \boldsymbol{a}^i}$, $\langle \cdot \rangle$ denotes the Macaulay brackets and tensor $\boldsymbol{n}$ is defined as

$$\boldsymbol{n} = \frac{\boldsymbol{P\xi}}{\sqrt{\boldsymbol{\xi P \xi}}} \tag{10}$$

The formulation of the kinematic hardening rule considered herein is very generic. As a result, numerous kinematic hardening rules proposed in the literature can be simulated by tuning properly the material parameters of the model. The left column of Table 2 shows six kinematic hardening rules that can be described by Eqs. (8, 9), whereas the right column describes the material parameters that need to be defined in each case.

Table 2: Kinematic hardening rules and the corresponding material parameters.

Kinematic hardening rule	Selected material parameters
Generic form	N, $\delta_i, \overline{a}_i, C_i, \gamma_i$
Armstrong and Frederick [25]	N=1, $\delta_1 = 1, \overline{a}_1 = 0, C_1, \gamma_1$
Bari and Hassan [24]	N=4, $\delta_i = \delta', \overline{a}_{1-3} = 0, \overline{a}_4, C_{1-4}, \gamma_{1-4}$
Chaboche [44]	N, $\delta_i = 1, \overline{a}_i = 0, C_i, \gamma_i$
Modified Chaboche [45]	N=4, $\delta_i = 1, \overline{a}_{1-3} = 0, \overline{a}_4, C_{1-4}, \gamma_{1-4}$
Burlet and Gailletaud [46]	N=1, $\delta_1 = 0, \overline{a}_1 = 0, C_1, \gamma_1$

3.2 Numerical implementation

The numerical integration of the constitutive model presented above and its implementation within a finite element environment is a key issue for efficient and accurate modeling. An implicit integration scheme has been developed, together with its consistent linearization moduli so that accuracy and quadratic convergence are guaranteed. Furthermore, the implicit numerical integration scheme is implemented in the general purpose finite element software ABAQUS [40] through a user material subroutine UMAT. Kinematic hardening is considered through (a) the classical hardening rule proposed by Chaboche [44], (b) its modified form proposed in a later paper by Chaboche [45] and (c), the kinematic hardening rule proposed more recently by Bari and Hassan [24].

In the present numerical scheme, Eqs. (1-10) are integrated implicitly within the time step $[t_n, t_{n+1}]$ using an Euler-backward integration scheme resulting in the following expressions:

$$\boldsymbol{\varepsilon}_{n+1} = \boldsymbol{\varepsilon}_n + \boldsymbol{\Delta\varepsilon} \tag{11}$$

$$\boldsymbol{\sigma}_{n+1} = \boldsymbol{M}\boldsymbol{\varepsilon}^e{}_{n+1} \tag{12}$$

$$\boldsymbol{\xi}_{n+1} = \boldsymbol{\sigma}_{n+1} - \boldsymbol{\alpha}_{n+1} \tag{13}$$

$$f_{n+1} = \sqrt{\boldsymbol{\xi}_{n+1}\boldsymbol{P}\boldsymbol{\xi}_{n+1}} - \sqrt{2/3}\, k(\varepsilon^q{}_{n+1}) \leq 0 \tag{14}$$

$$\boldsymbol{\varepsilon}^p{}_{n+1} = \boldsymbol{\varepsilon}^p{}_n + \Delta\lambda \boldsymbol{P}\boldsymbol{\xi}_{n+1} \tag{15}$$

$$\varepsilon^q{}_{n+1} = \varepsilon^q{}_n + \Delta\lambda\sqrt{2/3\, \boldsymbol{\xi}_{n+1}\boldsymbol{P}\boldsymbol{\xi}_{n+1}} \tag{16}$$

$$\boldsymbol{n}_{n+1} = \frac{\boldsymbol{P}\boldsymbol{\xi}_{n+1}}{\sqrt{\boldsymbol{\xi}_{n+1}\boldsymbol{P}\boldsymbol{\xi}_{n+1}}} \tag{17}$$

$$\boldsymbol{a}_{n+1} = \sum_{i=1}^{N} (\boldsymbol{a}^i{}_n + \Delta\boldsymbol{\alpha}^i) \tag{18}$$

where,

$$\Delta\boldsymbol{\alpha}^i = C_i\boldsymbol{\Delta\varepsilon}^p - \delta_i\gamma_i\boldsymbol{a}^i{}_{n+1}\langle 1 - \frac{\overline{a_i}}{f(\boldsymbol{a}^i{}_n)}\rangle \Delta\varepsilon^q$$
$$-\gamma_i(1-\delta_i)(\boldsymbol{a}^i{}_{n+1}\cdot\boldsymbol{n}_{n+1})\boldsymbol{n}_{n+1}\langle 1 - \frac{\overline{a_i}}{f(\boldsymbol{a}^i{}_n)}\rangle \Delta\varepsilon^q \tag{19}$$

The robustness of the numerical scheme is further increased by using the consistent linearization moduli computed as follows:

$$\frac{\partial\boldsymbol{\sigma}_{n+1}}{\partial\boldsymbol{\Delta\varepsilon}} = \boldsymbol{M}\frac{\partial}{\partial\boldsymbol{\Delta\varepsilon}}(\boldsymbol{\varepsilon}_{n+1} - \boldsymbol{\varepsilon}^p{}_n - \Delta\lambda\boldsymbol{P}\boldsymbol{\xi}_{n+1}) \tag{20}$$

More information on the integration algorithm and the consistent linearization methodology can be found in a recent publication by the authors [39].

3.3 Calibration of the plasticity model

The calibration of the hardening rules is a key issue, and should be performed with the use of appropriate material tests. Cyclic tests on strip specimens according to ASTM A370-80a standard [47], are extracted from elbows of the same batch, and are used to calibrate the three hardening models under consideration. The size of the gauge length is equal to 110mm × 25mm and the strip specimens are tested under strain-controlled and stress-controlled conditions to identify the cyclic hardening parameters and the uni-axial material ratcheting response. Preferably, the model proposed by Bari and Hassan [24] would require multi-axial material ratcheting experiments, but such tests are not available. For the proper selection of the material parameters in cyclic hardening and ratcheting, a trial and error procedure has been performed. The stabilized loop obtained from strain-controlled tests at 2.2% strain amplitude is used, while the ratcheting response is evaluated against uni-axial stress-controlled tests with load ratio R=−0.8. The following material hardening parameters, which are common in the three kinematic hardening rules, are selected

E= 2×10^5 (MPa); ν= 0.3

σ_y= 315(MPa); Q_∞= −50 (MPa); b= 80

C_{1-4}= 45,000; 11,500; 6,000; 2,700 (MPa)

γ_{1-4}= 650; 200; 190; 15

whereas, the additional parameters associated with each hardening model are selected as follows:

Chaboche [44]: δ′= 1; $\overline{a_4}$ = 0 (MPa)

Mod. Chaboche [45]: δ′= 1; $\overline{a_4}$ = 10 (MPa)

Bari and Hassan [24]: δ′= 0.85; $\overline{a_4}$ = 15 (MPa)

The resulting stress-strain plots and the ratcheting results obtained from material tests and numerical simulations are presented in Figure 2. In the strain-controlled response shown in Figure 2(a), all three hardening rules provide similar results and hence, a single line plot is used, denoted as "numerical" in Figure 2(a). All three models are also capable of predicting quite accurately the stress-controlled tests shown in Figure 2(b). For simplicity, in the remaining part of the paper, the hardening rules proposed by Chaboche [44], Chaboche [45] and Bari and Hassan [24] will be referred to as "CH1", "CH2" and "BH" respectively.

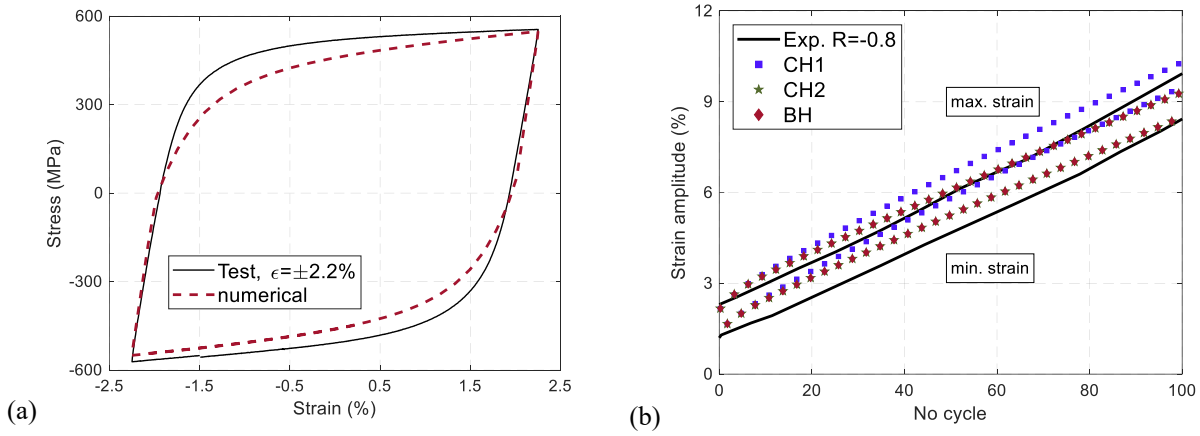

Figure 2: (a) Cyclic strain-stress curve for 2.2% strain amplitude and (b), material ratcheting response for R=−0.8.

4. Finite element model

A finite element model is developed to simulate the experimental procedure. Detailed information regarding the geometry of the assembly is shown in Figure 3, which illustrates the meshed finite element model employed. Double symmetry is considered with appropriate boundary conditions (Figure 3), allowing for modeling 1/4 of the specimen for computational efficiency. The model consists of a straight pipe segment and half of the pipe bend up to its central cross-section. It also accounts

for the actual thickness of the eblows, based on thickness measurements obtained before the tests. Those measurements indicated an average thickness of 9.1mm. Continuity conditions between the straight and the curve part are met through appropriate kinematic coupling of adjacent edges. In addition, a reference point (RP-1) is kinematically coupled with the free edge of the straight pipe to simulate the roller support and the capped-end conditions of the specimen. A sensitivity analysis was conducted to identify an optimized finite element mesh. The results of this sensitivity analysis indicated that a 10mm × 10mm mesh of linear quadrilateral shell elements with 5 integration points through the thickness is adequate for representing the stress and strain distribution at the elbow and obtain good results. The straight pipe is discretized using a single bias meshing technique, where the element size varies from 10mm × 10mm near the elbow bend to 10mm × 30mm near the capped end of the specimen.

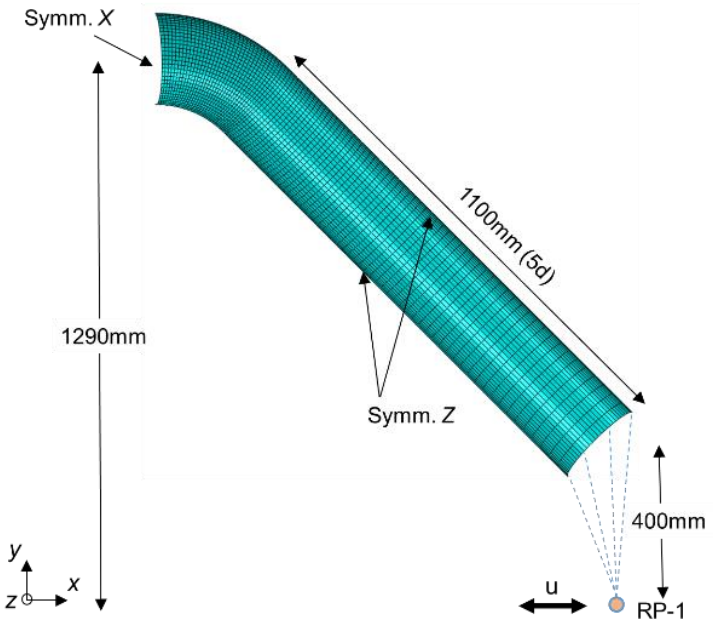

Figure 3: Finite element model of test specimen using plane stress (shell) elements.

5. Numerical simulation results

The results from the numerical simulation of the seven specimens (*E2-E8*) described in Table 1 are presented next. The scope of these analyses is to evaluate the capability of the numerical scheme equipped with the three advanced hardening models in simulating the experimental data on pipe elbows under low-cycle fatigue conditions. The present numerical simulation focuses on the cyclic elastoplastic response and ratcheting, whereas material degradation is not taken into account. It is noted that from the three hardening models considered herein only the model proposed by Chaboche [44] ("CH1" model) is available ("built-in") in a few commercial finite element packages (e.g. ABAQUS, ANSYS). Preliminary analyses with CH1

model, using the present UMAT subroutine and the "built-in" model of ABAQUS provided identical results, verifying the accuracy of the present scheme.

5.1 Force-displacement response

The accuracy of the numerical scheme equipped with the aforementioned advanced kinematic hardening rules is examined in terms of force-displacement response. Both experimental and the numerical analysis results indicate that upon saturation of cyclic hardening, the cyclic response stabilizes and does not change noticeably for a certain number of load cycles. Therefore, the stabilized hysteresis response of experiments *E2-E7* and the force amplitude obtained from specimen *E8*, tested under increasing displacement amplitude, are presented in Figure 4 and Figure 5. In terms of force-displacement response, the three hardening models provide negligible differences in their predictions and thus, a common plot is considered denoted as "numerical". It should be underlined that the additional features incorporated in the "CH2" and "BH" hardening models may not affect significantly the global structural response, especially during the initial loading cycles where plastic strains are relatively low. The good comparison between experimental data and numerical predictions shows that the present numerical scheme is capable of simulating quite accurately the inelastic response of the pipe elbow specimens under large amplitude inelastic cyclic loading.

5.2 Local strains

The accuracy of the numerical model is also examined by predicting the local strain range at several critical locations and its accumulation with respect to loading cycles. Pipe elbows, subjected to in-plane cyclic bending, ratchet multi-axially due to ovalization, while the maximum strains are observed in the hoop direction, and particularly at the elbow flank area. Numerical results are obtained at locations where hoop and longitudinal strains were measured during the experiments with the use of strain gauges. The accuracy of the numerical model is examined by comparing the experimental results with numerical predictions in terms of maximum and minimum strain values for a significant number of cycles.

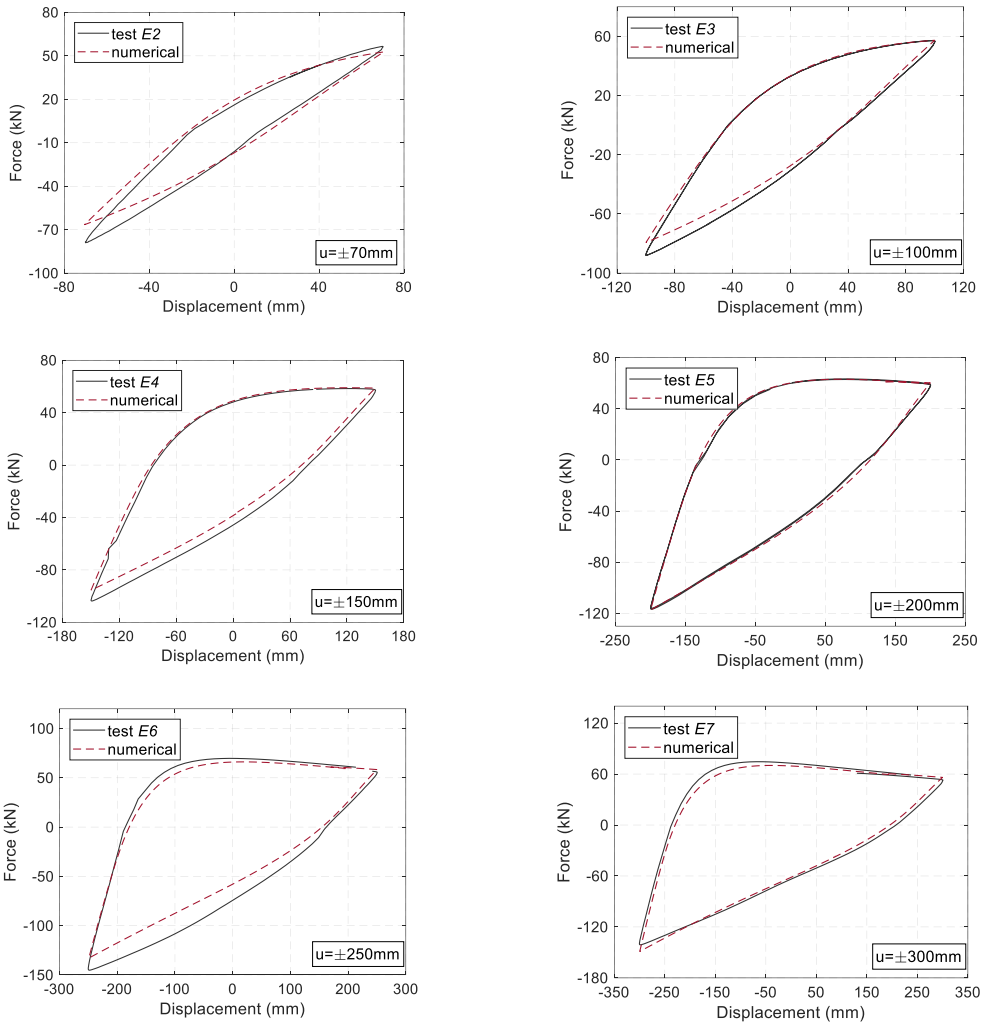

Figure 4: Experimentally and numerically obtained force-displacement response of specimens *E2-E7*.

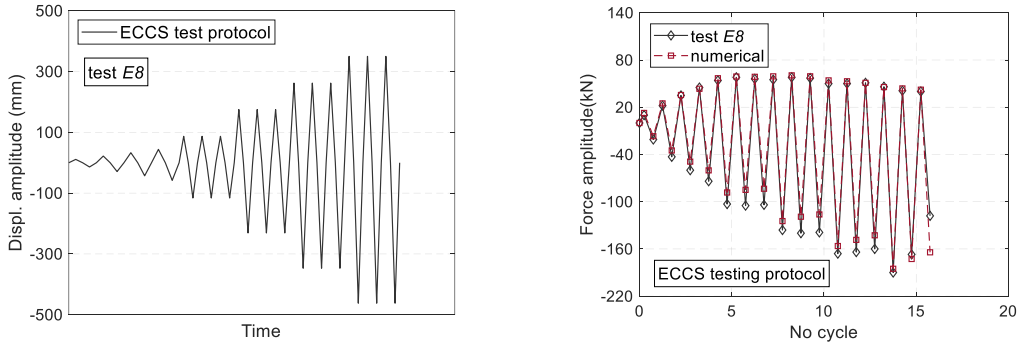

Figure 5: Experimentally and numerically obtained force amplitude of specimen *E8*.

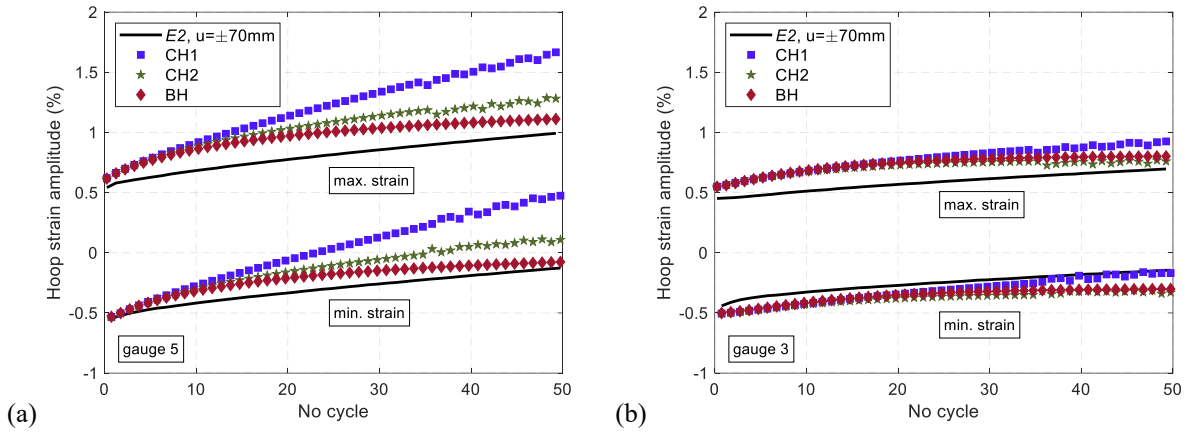

Figure 6: Hoop strain evolution observed at the elbow flank of specimen *E2*.

In specimen *E2*, subjected to displacement amplitude of ±70mm, hoop strain measurements obtained at gauge 3 and gauge 5 (see Figure 1) are examined. Figure 6 shows that hardening model "CH1" over-predicts material ratcheting. Larger differences are observed at the flank location (Figure 6a), which become less significant when focusing on gauge 3 and the corresponding predictions (Figure 6b). Hardening models "CH2" and "BH" provide more accurate predictions. In particular the "BH" model provides the most accurate predictions in comparison with the experimental measurements. With respect to measurements of longitudinal strain obtained at the intrados and the extrados of the pipe elbow (Figure 7), the measured strains are rather low and exhibit negligible ratcheting, so that the three models appear to provide satisfactory results.

The analysis of specimen *E3* (Figure 8) subjected to displacement amplitude of ±100mm shows that the differences in the results obtained with the three hardening models follow the same trends observed in specimen *E2*. However, in this case, the differences between "CH2" and "BH" become more pronounced. In addition, the "BH" model provides the most accurate predictions with respect to experimental data.

Specimen *E4* has been subjected to displacement amplitude of ±150mm, and hoop strain measurements have been interrupted in less than 20 load cycles due to large values of strain and failure of the strain gauge. Longitudinal strain measurements at extrados are provided for the first 50 cycles, but no measurements have been obtained at elbow intrados due to strain gauge detachment at early stage of testing. The strain gauge 5, located exactly at the crown location, detached quite early, at the 7th load cycle (Figure 9a), whereas gauge 4 failed after 18 cycles. In both cases, the superiority of the advanced hardening models "CH2" and "BH" over the more conventional model "CH1" is obvious, even within the above limited number of load cycles. Model "CH1" predicts fairly well the minimum strain in every load cycle but over-predicts the value of the strain range. A minor over-prediction of the induced strain range is also observed in the results of model "BH", which is

associated with an under-prediction of the minimum induced strain. A similar trend is observed in Figure 10, which shows the evolution of the longitudinal strains at the extrados location. The results obtained with the use of "CH2" and "BH" models are close to the experimental measurements, while model "CH1" over-predicts significantly the maximum strain. Furthermore, the strain ratcheting and the gradual reduction of ratcheting rate predicted by the "BH" model is in good agreement with the corresponding experimental data, as shown in Figure 9 and Figure 10.

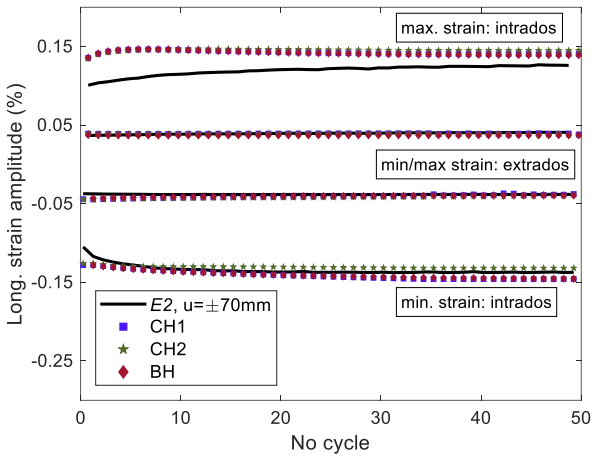

Figure 7: Longitudinal strain evolution observed at the intrados and extrados of specimen *E2*.

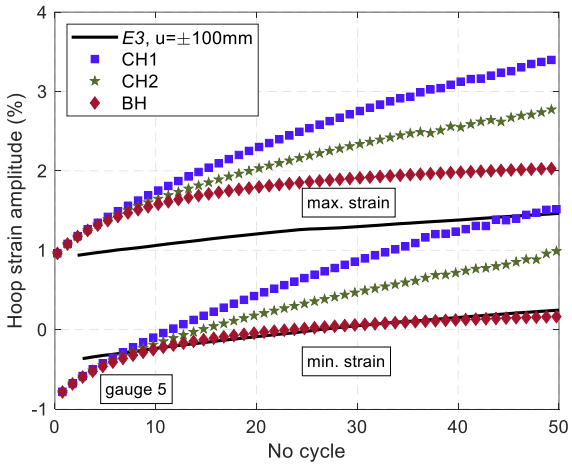

Figure 8: Hoop strain range evolution observed at the elbow flank of specimens *E3*.

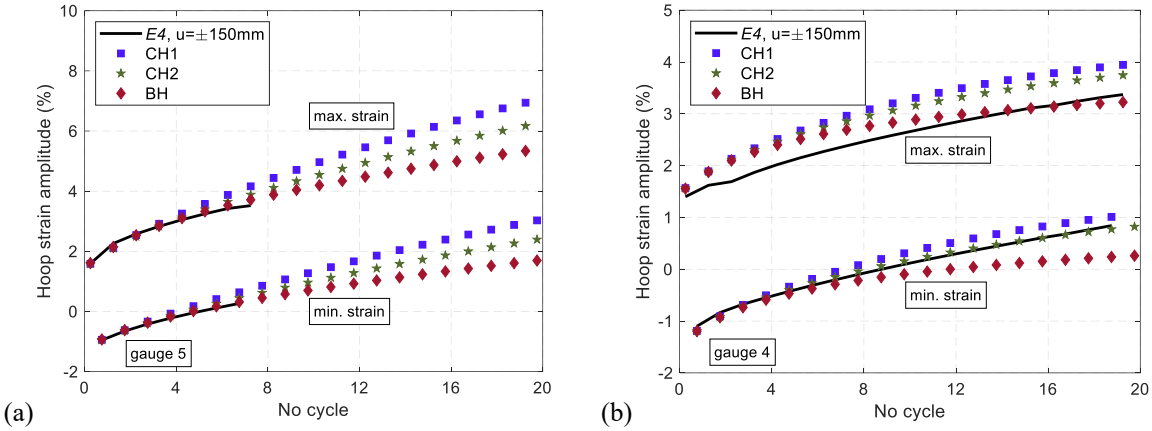

Figure 9: Hoop strain evolution observed at the elbow flank of specimens *E4*.

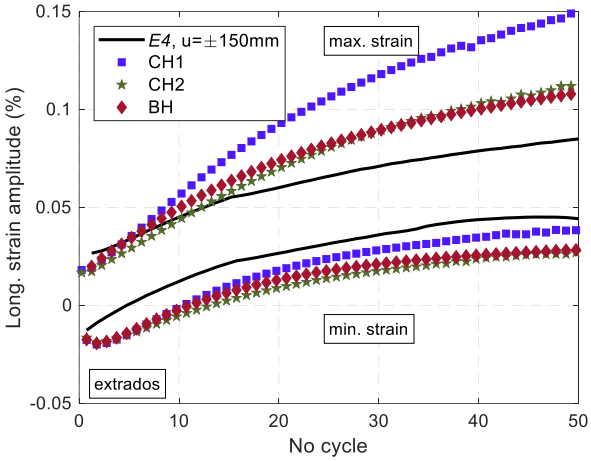

Figure 10: Longitudinal strain evolution observed at the extrados of specimens *E4*.

Strain measurements in specimen *E5* are not available exactly at the crown location due to early failure of the corresponding strain gauge, and comparisons of the numerical predictions with strain readings from gauge 3 are shown in Figure 11. As expected, ratcheting is less severe at this location and the corresponding strain amplitudes are limited to $\pm 2.5\%$ regardless of the large induced displacements. The results obtained from the three hardening models have similar accuracy with respect to the experimental results, whereas model "BH" provides better accuracy on the value of the maximum induced hoop strain in every load cycle. Contour plots illustrating the distribution of hoop strains on the inner and the outer surface of specimen *E5* during the frist load cycle are presented in Figure 12. These contour plots are obtained with "BH" model and correspond to the stages of maximum closing and maximum opening displacement. The location of maximum hoop strain at the inner and the

outer surface of the elbow is observed. In addition, Figure 13 shows the evolution of the equivalent plastic strain (denoted as SDV7 in UMAT) at the outer surface of the pipe bend, during the first 28 load cycles.

Hoop strain accumulation at the elbow flank area of specimens *E6-E8* has also been obtained, and is presented in Figure 14 - Figure 16. In these experiments, applied displacement amplitude is significantly high and the specimens failed under low-cycle fatigue with a through-thickness crack in less than 16 load cycles. The available experimental data for local strain are very limited, because the majority of the strain gauges reached their capacity or detached from the pipe quite early during testing of those specimens. Figure 14 and Figure 15 show that the numerical models simulate the maximum strain in specimens *E6* and *E7* accurately, but fail to predict accurately the evolution of the minimum strain over the load cycles. This discrepancy is attributed to the gradual detachment of the strain gauges from the pipe elbow surface. Numerical results obtained from specimen *E8*, subjected to an increasing amplitude loading protocol [48], are also provided in Figure 16. The numerical results compare very well with the experimental measurements, demonstrating the accuracy and the efficiency of the numerical scheme.

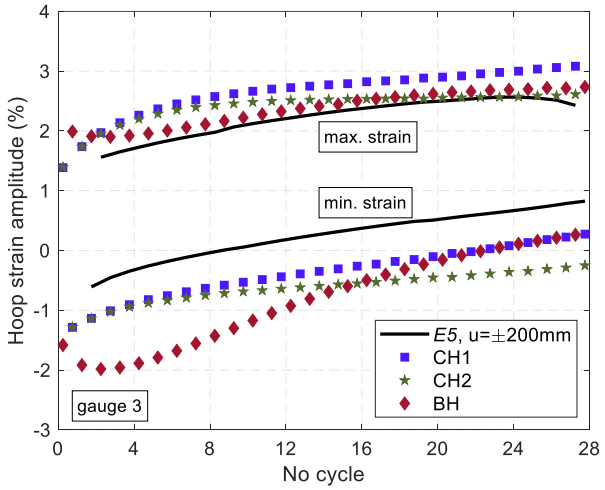

Figure 11: Hoop strain evolution observed near the elbow flank of specimens *E5*.

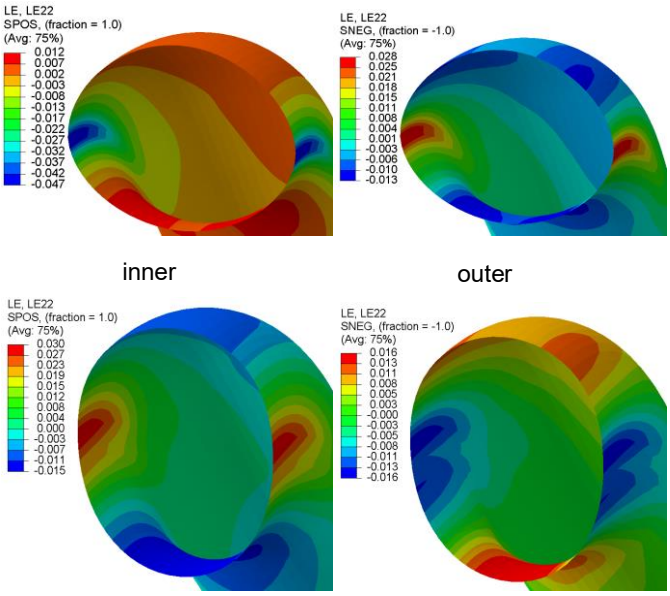

Figure 12: Distribution of hoop strain at inner and outer surface at the maximum closing/opening displacement of specimen *E5* at the first loading cycle (hardening model "BH").

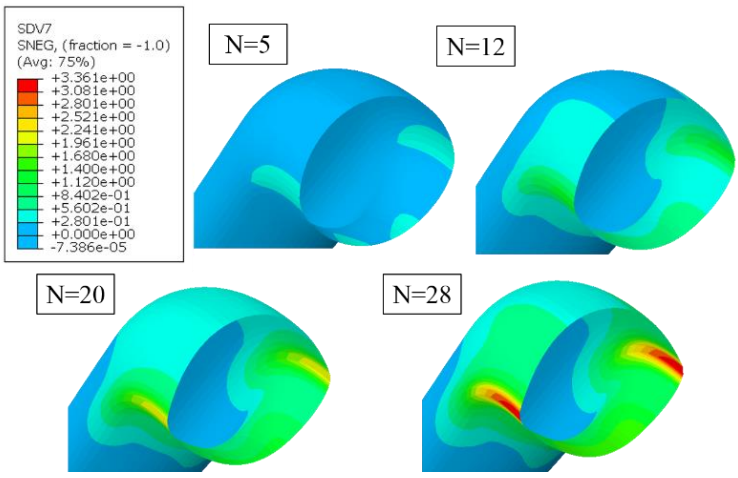

Figure 13: Evolution of plastic hoop strain in specimen *E5* over the load cycles, obtained with the use of "BH" hardening model.

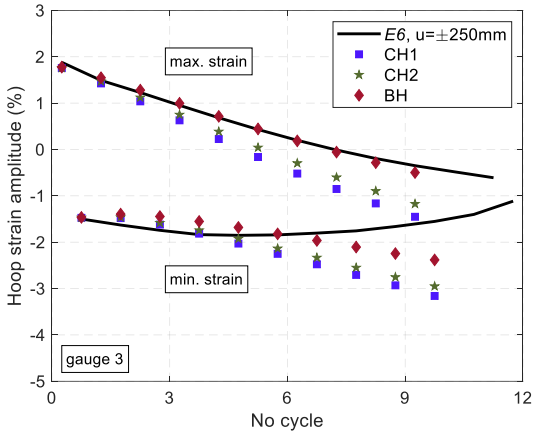

Figure 14: Hoop strain evolution observed near the elbow flank of specimens *E6*.

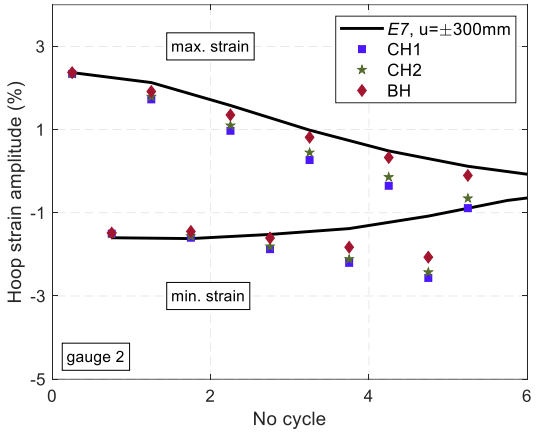

Figure 15: Hoop strain evolution observed near the elbow flank of specimens *E7*.

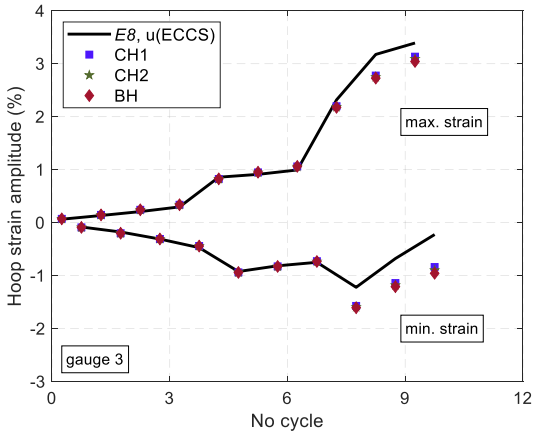

Figure 16: Hoop strain evolution observed near the elbow flank of specimens *E8*.

5.3 Ovalization

In addition to strains, numerical predictions in terms of cross-sectional ovalization are also presented. A special apparatus has been used to measure the change of diameter in the vertical direction at the crown location (Dv_c) during the experiments [41]. Figure 17 shows the normalized flattening values ("ovalization") obtained both experimentally and numerically through the simulation of tests *E2-E7.* The ovalization values are expressed by the following dimensionless ovalization parameter:

$$Ov_c = \frac{D - Dv_c}{D} \tag{21}$$

where D is the nomimal diameter and Dv_c is the distance between pipe elbow intrados and extrados at the stage of maximum opening/closing displacement. Figure 17 shows that the increase of applied displacement amplitude leads to higher ovalization. Furthermore, the ovalization values increase only slightly with respect to the loading cycles, an observation verified by both the experimental data and the numerical results, obtained from all three hardening models. Therefore, the corresponding ovalization values are plotted in the bar-chart of Figure 17 in one bar, denoted as "numerical". The chart shows that ovalization of specimens *E2-E7* depends on the loading amplitude and ranges between 3% and 15% for the cases examined in the present work. Furthermore, minor differences are observed between the maximum closing and opening ovalization values in both cases. The good comparison between the numerical results and the experimental data shows that the numerical scheme equipped with the three hardening rules under consideration is capable of providing quite satisfactory predictions of pipe elbow ovalization.

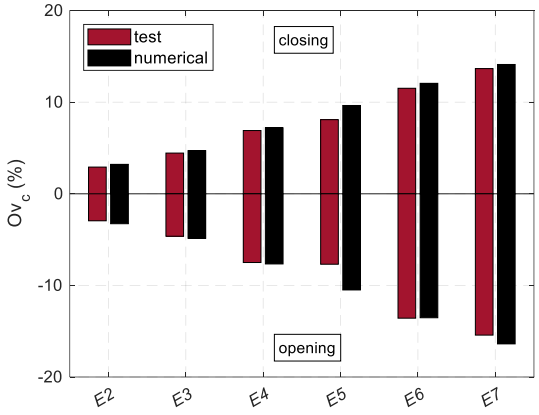

Figure 17: Experimentally and numerically obtained ovalization values of specimens *E2-E7.*

6. Conclusions

Numerical simulation of a set of large-scale experiments on steel pipe elbows under in-plane cyclic bending is performed, using advanced finite element tools. Material constitutive modeling is based on J_2 plane stress cyclic elasto-plasticity with mixed nonlinear hardening. The numerical scheme is implemented in a finite element environment through an unconditionally stable implicit integration scheme, within a user material subroutine, extensively discussed in a recent publication of the authors [39]. Three advanced hardening models are selected for simulating the experiments. From the three models, only the hardening model "CH1" may be available as "built-in" model in commercial finite element packages.

Comparisons between experimental data and numerical results are performed in terms of force-displacement response, cross-sectional ovalization and in particular local strains, with emphasis on ratcheting. The results show that the finite element model equipped with the material user-subroutine could simulate accurately the inelastic force-displacement response obtained from the elbow experiments. With respect to cross-sectional ovalization, examined at the middle cross-section, the numerical results obtained with the three hardening rules and the experimental data compare very well in terms of its amplitude, despite a small over-prediction observed for large values of applied displacement. Model "CH1" is more primitive and does not provide accurate predictions of hoop strain at the elbow flank, and axial strain ratcheting at the extrados and the intrados. The over-prediction of ratcheting rate by the "CH1" model, and its inability to simulate uni-axial and multi-axial ratcheting shakedown, is in agreement with the conclusions of previous works [32,35]. The results obtained with models "CH2" and "BH" are in better agreement with the experimental data. Furthermore, the improved accuracy observed in "BH" model in comparison to "CH2" is attributed to the multi-axial ratcheting parameter δ' in the former model which allows prediction of ratcheting shakedown under multi-axial conditions. Overall, considering both axial and hoop strain measurements, model "BH" provides the best accuracy in terms of ratcheting prediction among the three models under consideration. As a general conclusion, accurate prediction of elasto-plastic response of pipe elbows constitutes a challenging task, mainly due to the presence of ratcheting. The consideration of less elaborate and more conventional hardening models, such as "CH1", may result in overestimating the strain evolution rate, possibly leading to conservative design. On the other hand, more elaborate hardening models, such as "BH", provide improved predictions towards more efficient design of pipe elbows. Finally, the very good comparison between experimental data and numerical results demonstrates that the developed numerical scheme, formulated specifically for plane stress conditions, offers a computationally efficient numerical tool for simulating the mechanical response of piping components and for assessing their integrity under severe loading conditions.

Nomenclature

$\boldsymbol{\varepsilon}/\boldsymbol{\varepsilon}^e/\boldsymbol{\varepsilon}^p$	total/elastic/plastic strain tensor
$\boldsymbol{\sigma}$	stress tensor
$\boldsymbol{M}$	elastic constitutive matrix
$\boldsymbol{P}$	projection matrix
$\boldsymbol{\alpha}$	kinematic hardening tensor
C_i/γ_i	kinematic hardening parameters
δ_i	Multi-axial ratcheting parameter
$\overline{a_i}$	threshold term
$k(\varepsilon_q)$	isotropic hardening function
ε_q	equivalent plastic strain
σ_y	yield strength
Q / b	isotropic hardening parameters
$\boldsymbol{n}$	outward to the yield surface vector
D	Pipe outer diameter
R	Radius of bend

Acknowledgements

The authors would like to thank the School of Engineering, The University of Edinburgh, Scotland, UK for supporting this research project through a PhD fellowship to the first author.

References

[1] EPRI, Piping and fitting dynamic reliability program, Vol. 2-Component Test Report, EPRI Contract No. RP 1543-15, (1992).

[2] EPRI, Fatigue management handbook, Vol. 2-fatigue screening criteria, EPRI contract No. TR-104534-V2, (1994).

[3] R.J. Rider, S.J. Harvey, H.D. Chandler, Fatigue and ratcheting interactions, Int. J. Fatigue. 17 (1995) 507–511. https://doi.org/10.1016/0142-1123(95)00046-V.

[4] X. Lu, Influence of residual stress on fatigue failure of welded joints, North Carolina State University, 2003.

[5] E. Wei, B. Postberg, T. Nicak, J. Rudolph, Simulation of ratcheting and low cycle fatigue, Int. J. Press. Vessel. Pip. 81 (2004) 235–242. https://doi.org/10.1016/J.IJPVP.2004.01.002.

[6] P.K. Shaw, S. Kyriakides, Inelastic analysis of thin-walled tubes under cyclic bending, Int. J. Solids Struct. 21 (1985) 1073–1100. https://doi.org/10.1016/0020-7683(85)90044-7.

[7] E. Corona, S. Kyriakides, An experimental investigation of the degradation and buckling of circular tubes under cyclic bending and external pressure, Thin-Walled Struct. 12 (1991) 229–263. https://doi.org/10.1016/0263-8231(91)90048-N.

[8] D.N. Moreton, K. Yahiaoui, D.G. Moffat, Onset of ratchetting in pressurised piping elbows subjected to in-plane bending moments, Int. J. Press. Vessel. Pip. 68 (1996) 73–79.

[9] K. Yahiaoui, D.G. Moffat, D.N. Moreton, Response and cyclic strain accumulation of pressurized piping elbows under dynamic in-plane bending, J. Strain Anal. Eng. Des. 31 (1996) 135–151.

[10] K. Yahiaoui, D.N. Moreton, D.G. Moffat, Response and cyclic strain accumulation of pressurized piping elbows under dynamic out-of-plane bending, J. Strain Anal. Eng. Des. 31 (1996) 153–166.

[11] G.C. Slagis, Experimental data on seismic response of piping components, J. Press. Vessel Technol. 120 (1998) 449–455. https://doi.org/10.1115/1.2842358.

[12] K. Suzuki, Y.Y. Namita, H.H. Abe, Seismic proving test of ultimate piping strength: Current status of preliminary tests-II, ASME. Int. Conf. Nucl. Eng. 10th Int. Conf. Nucl. Eng. 1 (2002) 573–580. https://doi.org/10.1115/ICONE10-22225.

[13] X. Chen, B. Gao, G. Chen, Ratcheting study of pressurized elbows subjected to reversed in-plane bending, ASME. J. Press. Vessel Technol. 128 (2005) 525–532. https://doi.org/10.1115/1.2349562.

[14] H. Shi, G. Chen, Y. Wang, X. Chen, Ratcheting behavior of pressurized elbow pipe with local wall thinning, Int. J. Press. Vessel. Pip. 102–103 (2013) 14–23.

[15] S. Vishnuvardhan, G. Raghava, P. Gandhi, M. Saravanan, S. Goyal, P. Arora, S.K. Gupta, V. Bhasin, Ratcheting failure of pressurised straight pipes and elbows under reversed bending, Int. J. Press. Vessel. Pip. 105–106 (2013) 79–89. https://doi.org/10.1016/J.IJPVP.2013.03.005.

[16] G.E. Varelis, S.A. Karamanos, A.M. Gresnigt, Pipe elbows under strong cyclic loading, J. Press. Vessel Technol. 135 (2013) 11207–11209. https://doi.org/10.1115/1.4007293.

[17] G.E. Varelis, S.A. Karamanos, Low-cycle fatigue of pressurized steel elbows under in-plane bending, J. Press. Vessel Technol. 137 (2015) 11401–11410. https://doi.org/10.1115/1.4027316.

[18] C. Liu, D. Yu, W. Akram, Y. Cai, X. Chen, Ratcheting behavior of pressurized elbow pipe at intrados under different loading paths, Thin-Walled Struct. 138 (2019) 293–301. https://doi.org/10.1016/J.TWS.2019.02.013.

[19] A. Rahmatfam, M. Zehsaz, T.N. Chakherlou, Ratcheting assessment of pressurized pipelines under cyclic axial loading: Experimental and numerical investigations, Int. J. Press. Vessel. Pip. 176 (2019) 103970. https://doi.org/10.1016/J.IJPVP.2019.103970.

[20] M. Foroutan, G.R. Ahmadzadeh, A. Varvani-Farahani, Axial and hoop ratcheting assessment in pressurized steel elbow pipes subjected to bending cycles, Thin-Walled Struct. 123 (2018) 317–323. https://doi.org/10.1016/J.TWS.2017.11.021.

[21] X. Chen, X. Chen, D. Yu, B. Gao, Recent progresses in experimental investigation and finite element analysis of ratcheting in pressurized piping, Int. J. Press. Vessel. Pip. 101 (2013) 113–142. https://doi.org/10.1016/J.IJPVP.2012.10.008.

[22] S. Bari, T. Hassan, Anatomy of coupled constitutive models for ratcheting simulation, Int. J. Plast. 16 (2000) 381–409. https://doi.org/10.1016/S0749-6419(99)00059-5.

[23] S. Bari, T. Hassan, Kinematic hardening rules in uncoupled modeling for multiaxial ratcheting simulation, Int. J. Plast. 17 (2001) 885–905. https://doi.org/10.1016/S0749-6419(00)00031-0.

[24] S. Bari, T. Hassan, An advancement in cyclic plasticity modeling for multiaxial ratcheting simulation, Int. J. Plast. 18 (2002) 873–894. https://doi.org/10.1016/S0749-6419(01)00012-2.

[25] P.J. Armstrong, C.O. Frederick, A mathematical representation of the multiaxial Bauschinger effect, Mater. High Temp. 24 (1966) 1–26. https://doi.org/10.1179/096034007X207589.

[26] A.B. Ayob, D.G. Moffat, J. Mistry, The interaction of pressure, in-plane moment and torque loadings on piping elbows, Int. J. Press. Vessel. Pip. 80 (2003) 861–869. https://doi.org/10.1016/J.IJPVP.2003.09.001.

[27] C. Balan, D. Redektop, The effect of bidirectional loading on fatigue assessment of pressurized piping elbows with local thinned areas, Int. J. Press. Vessel. Pip. 81 (2004) 235–242.

[28] C.-S. Oh, Y.-J. Kim, C.-Y. Park, Shakedown limit loads for elbows under internal pressure and cyclic in-plane bending, Int. J. Press. Vessel. Pip. 85 (2008) 394–405. https://doi.org/10.1016/J.IJPVP.2007.11.009.

[29] N.T. Tseng, G.C. Lee, Simple plasticity model of the two surface type, J. Eng. Mech. ASCE. 109 (1983) 795–810.

[30] T. Hassan, S.M. Rahman, Simulation of ratcheting responses of elbow piping components, in: ASME. Press. Vessel. Pip. Conf. Vol. 1 Codes Stand., 2008: pp. 103–108. https://doi.org/103-108. doi:10.1115/PVP2009-77819.

[31] S.M. Rahman, T. Hassan, E. Corona, Evaluation of cyclic plasticity models in ratcheting simulation of straight pipes under cyclic bending and steady internal pressure, Int. J. Plast. 24 (2008) 1756–1791. https://doi.org/10.1016/j.ijplas.2008.02.010.

[32] T. Hassan, M. Rahman, Constitutive models in simulating Low-Cycle fatigue and ratcheting responses of elbow, ASME. J. Press. Vessel Technol. 137 (2015) 031002.

[33] T. Hassan, M. Rahman, S. Bari, Low-cycle fatigue and ratcheting responses of elbow piping components, ASME. J. Press. Vessel Technol. 137 (2015) 031010-031010–12. https://doi.org/doi:10.1115/1.4029068.

[34] N. Ohno, J.D. Wang, Kinematic hardening rules with critical state of dynamic recovery, part I and II, Int. J. Plast. 9 (1993) 375–390. https://doi.org/https://doi.org/10.1016/0749-6419(93)90042-O.

[35] N. Islam, T. Hassan, Development of a novel constitutive model for improved structural integrity analysis of piping components, Int. J. Press. Vessel. Pip. 177 (2019) 103989. https://doi.org/10.1016/J.IJPVP.2019.103989.

[36] M.A. Fenton, Low-cycle fatigue failure and ratcheting responses of short and long radius elbows at room and high temperatures, MSc Thesis NC State University, 2014.

[37] P. Sollogoub, The OECD-NEA Programme on metallic component margins under high seismic loads (MECOS): Towards new criteria, in: Proc. ASME 2017 Press. Vessel. Pip. Conf., 2017: pp. PVP2017-65516.

[38] P.B. Labbé, G.R. Reddy, C. Mathon, F. Moreau, S.A. Karamanos, The OECD-NEA programme on metallic component margins under high seismic loads (MECOS), in: Proc. ASME 2016 Press. Vessel. Pip. Conf., 2016: pp. PVP2016-63119.

[39] K. Chatziioannou, S.A. Karamanos, Y. Huang, An implicit numerical scheme for cyclic elastoplasticity and ratcheting under plane stress conditions, Comput. Struct. (2019).

[40] ABAQUS, Standards user's manual, Version 2016. Hibbitt, SImulia and Sorensen, Inc., 1997, Dassault Systems, (2016).

[41] P. Pappa, G.E. Varelis, M. Vathi, P.C. Perdikaris, S.A. Karamanos, J. Ferino, A. Lucci, E. Mecozzi, G. Demofonti, Structural safety of industrial steel tanks, pressure vessels and piping systems under seismic loading, Final report, INDUSE RFCS project, 2012.

[42] ASME B16.9, Factory-made wrought butt welding fittings, 2007.

[43] J.C. Simo, R.L. Taylor, A return mapping algorithm for plane stress elastoplasticity, Int. J. Numer. Methods Eng. 22 (1986) 649–670. https://doi.org/10.1002/nme.1620220310.

[44] J.L. Chaboche, Time-independent constitutive theories for cyclic plasticity, Int. J. Plast. 2 (1986) 149–188. https://doi.org/http://dx.doi.org/10.1016/0749-6419(86)90010-0.

[45] J.L. Chaboche, On some modifications of kinematic hardening to improve the description of ratchetting effects, Int. J. Plast. 7 (1991) 661–678. https://doi.org/10.1016/0749-6419(91)90050-9.

[46] H. Burlet, G. Cailletaud, Numerical techniques for cyclic plasticity at variable temperature, Eng. Comput. 3 (1986) 143–153. https://doi.org/10.1108/eb023652.

[47] ASTM A370-80a, Standard Test Methods and Definitions for Mechanical Testing of Steel Products, 2016.

[48] ECCS, Recommended testing procedure for assessing the behavior of structural steel elements under cyclic loads, 1968.